# A New Method for the Accurate Prediction of On-Load Power Factor in Two-Pole Induction Motors Considering Shaft Eddy Currents

Matteo Olivo, Mauro Bortolozzi, Alberto Tessarolo ⓘ, *Senior Member, IEEE*, and Fabio Luise

*Abstract*—An accurate prediction of medium-voltage induction motor (IM) power factor in rated conditions is important in the design stage to verify the machine compliance with specifications according to international testing standards. Laboratory and industrial experiences suggest that significant errors in full-load power factor calculation can result for two-pole IMs in particular, due to the eddy currents induced in the solid-steel shaft at rated slip. Such eddy currents are responsible for rejecting the main flux into rotor laminated yokes causing an increase in their saturation and, hence, in the required magnetizing current with respect to no-load conditions. This article proposes a method to study the phenomenon through a combination of analytical and simplified Finite Element (FE) calculations as a computationally-efficient alternative to conventional FE simulations. The results of the proposed approach are experimentally assessed by comparison with measurements on a set of built and tested medium-voltage two-pole IMs of different sizes, showing very good accuracy and computational performance.

*Index Terms*—Design, electric machines, finite element analysis, induction motors, power factor, shaft currents.

## I. INTRODUCTION

INDUCTION motors have been the most widespread option in the industrial electric drive field for several decades [1]. They can be preferable to synchronous machines thanks to their high reliability [2] and low cost, but suffer for a relatively poor efficiency [3], [4] and power factor [5].

Power factor plays a key role in determining an IM performance as it closely relates to its electric power consumption over time [5]. An accurate prediction of full-load power factor is an essential task in IM design also because international standards prescribe tight tolerances on its measured value with respect to specifications [6].

Matteo Olivo and Alberto Tessarolo are with the University of Trieste, 34127 Trieste, Italy (e-mail: matteo.olivo@phd.units.it; atessarolo@units.it).

Mauro Bortolozzi is with Rete Ferroviaria Italiana, 34135 Trieste, Italy (e-mail: mbortolozzi@rfi.it).

Fabio Luise is with NIDEC Industrial Solutions, 34074 Monfalcone, Italy (e-mail: fabio.luise@nidec-asi.com).

The accurate power factor estimation is particularly critical in two-pole IMs, where the main flux flowing through the rotor tends to enter the shaft, which is typically made of solid steel. At no load the magnetic field revolves almost synchronously with the rotor, so that no voltages and currents are induced in it. Conversely, when the motor is loaded, the relative motion (slip) between the main flux and the rotor induces eddy currents in the solid-steel shaft [7]. As a consequence, flux lines are partly rejected from the solid steel and forced to enter the laminated rotor yokes [8], [9], which are thus subjected to a higher magnetic saturation than in no-load conditions. This causes the full-load magnetizing current to be larger than the no-load one and thus leads to a worse power factor than can be predicted with usual analytical [10], [11], numerical [12] or hybrid [13] IM calculation methods.

Shaft eddy-currents and their effect on rotor magnetic field distribution have been already investigated in the literature, using both FE simulations of the entire motor [7] and analytical methods [8], [9]. FE approaches suffer from the known drawback of being time-consuming, while analytical techniques, although fast, rely on simplifying heuristic assumptions that may compromise their accuracy and generality. For instance, they are typically incapable of accounting for axial cooling vents in the rotor core [7] or for strongly non-uniform flux density distributions in the rotor yoke and shaft [8], [9].

To help overcome the mentioned issues, a new procedure for power factor calculation in three-phase two-pole medium-voltage IMs is presented in this paper. The method combines the time-harmonic FE Analysis (FEA) of an easy-to-solve reduced IM model with analytical calculations based on motor equivalent circuit [13]. The purpose is to achieve a good compromise between accuracy and generality on one side and computational efficiency on the other.

The paper is organized as follows. An insight into the physics of the problem is first given in Section II though experiments on a specifically designed laboratory prototype. Section III discusses IM full-load power-factor prediction by means of time-harmonic FE simulations applied to the whole machine 2D model. Section IV illustrates the new proposed procedure, where the whole 2D model is replaced by a suitably reduced one. Finally, Section V experimentally validates the method on a set of built and tested two-pole IMs of different sizes, in order to quantify its precision and computational burden.
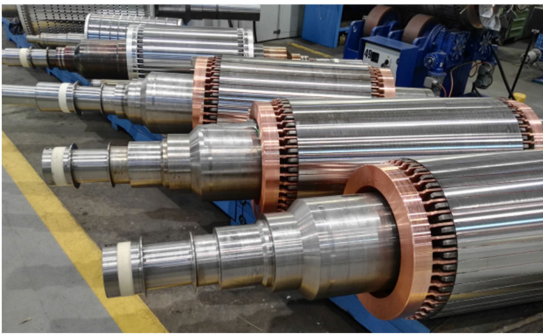
Fig. 1. Rotors of medium-voltage two-pole squirrel-cage IMs with laminated core and solid-steel shaft (courtesy of Nidec Industrial Solutions, Monfalcone, Italy).



Fig. 3. Laboratory test equipment for investigating shaft eddy current impact on the magnetizing current: (a) variable-speed driven shaft; (b) special prototype for test; (c) digital wattmeter; (d) electric power supply; (e) prototype rotor core; (f) prototype solid-steel shaft.

<center>TABLE I</center>
<center>PROTOTYPE MACHINE DATA</center>

| Stator outer diameter | 240 mm | Laminations material | M530-65A [a] |
|---|---|---|---|
| Stator bore diameter | 148 mm | Solid shaft material | C40 [b] |
| Air gap width | 0.5 mm | Nr. of stator slots | 36 |
| Rotor yoke thickness | 20.2 mm | Nr. of series turns per phase | 60 |
| Core length | 150 mm | Nr. of parallel paths per phase | 1 |
| Shaft diameter | 38 mm | Stator coil pitch | 5/6 |
| Number of poles | 2 | Stator phase connection | Y |
| Rated voltage | 380 V | Magnetizing current by design | 7A |

[a] According to standard EN 10106
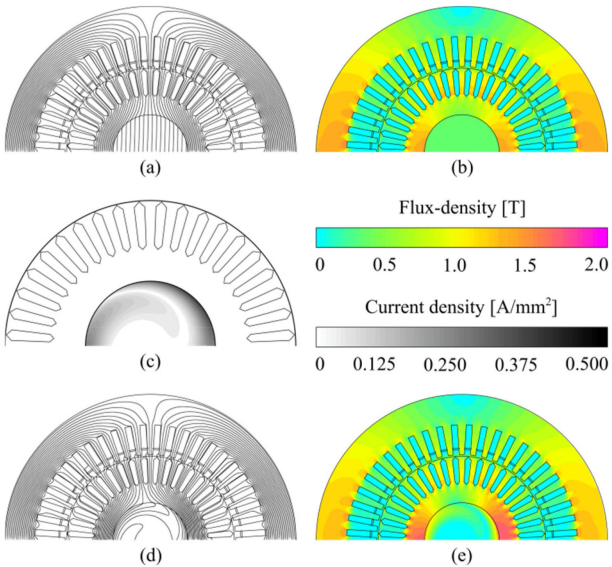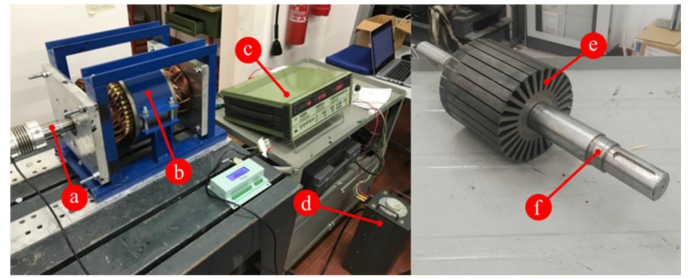[b] According to standard ISO 683-1



Fig. 2. Magnetic flux and eddy current distribution in a two-pole IM. (a) Flux lines and (b) flux-density at no load; (c) shaft eddy-current density, (d) flux lines and (e) flux density at full load.

## II. PHYSICS OF THE PROBLEM

### A. Description of the Phenomenon

The shaft of electric machines is usually not classified as an active part, but rather treated as an electromagnetically passive mechanical component. However, for two-pole IMs, which typically include a laminated rotor core and a solid-steel shaft (Fig. 1), the situation is different. In these machines, when operated at no load, the main flux tends to cross the shaft as illustrated in Fig. 2-a, encountering a relatively low reluctance and requiring a given magnetizing current. When the motor is loaded, instead, the relative motion between the rotating field and the rotor causes eddy currents in the shaft as shown in Fig. 2-c; these tend to partly reject the flux lines into the laminated rotor yokes (Fig. 2-d) causing an increase in their magnetic saturation as it can be observed by comparing Fig. 2-b and Fig. 2-e. As a consequence, the main flux encounters a higher reluctance at full load on crossing the rotor and requires a larger magnetizing current than at no load. Such variation in the magnetizing current

as a function of the slip (from no-load to loaded conditions) is usually neglected in the performance calculation of IMs [10]–[13], while it may have a significant entity as experimentally investigated in the next subsection.

### B. Experimental Investigations on a Laboratory Prototype

Some laboratory tests are carried out, using the equipment shown in Fig. 3, on a special electric machine prototype having a solid steel shaft and a laminated rotor core without any kind of squirrel cage or winding (Fig. 3-b). The main prototype data are given in Table I. The stator has a usual design with a three-phase winding fed from a 50 Hz adjustable-voltage source. The rotor is coupled to a prime mover supplied through a variable-frequency drive (VFD). This testing arrangement allows to change the rotor speed while the stator supply frequency is constant, so as to obtain the desired slip values. Due to the absence of rotor circuits, the machine mainly absorbs its magnetizing current at steady state, except for a small active current component required to sustain core and stator winding losses.

By adjusting the rotor speed through the prime mover, the prototype is forced to operate at different slips and, for any given slip, the voltage-versus-current characteristic is measured by varying the stator supply voltage. The experimental results of the test are shown in Fig. 4 for slip values between 0 and 1.2%. It can be noticed how, as the slip increases, the magnetizing current drawn for a given voltage (i.e., motor flux) grows. The fact can be more clearly observed by plotting the current-versus-slip characteristics for different voltages as shown in Fig. 5. For instance, Fig. 5 shows that the magnetizing current for a terminal voltage of 400 V grows by 23% as the slip increases from 0 to
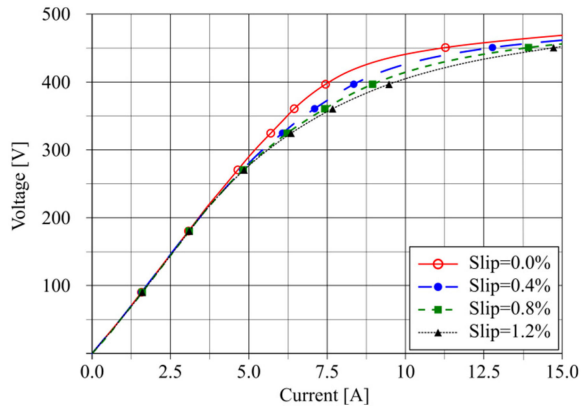
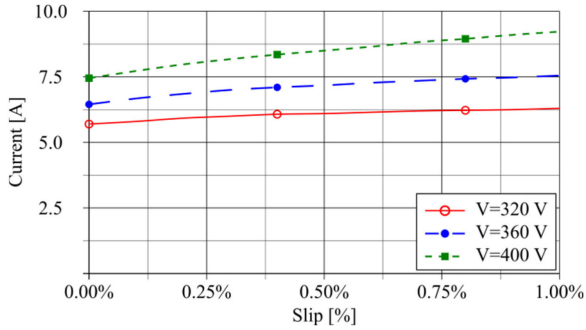Fig. 4. Voltage-versus-current characteristics measured at different slips.



Fig. 5. Measured magnetizing current variation with the slip for different terminal voltages.
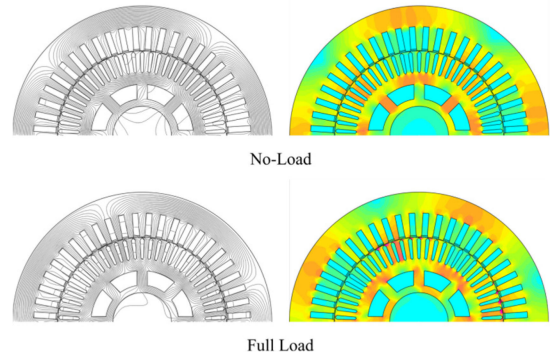


Fig. 6. Magnetic flux lines and color map for a four-pole IM in no-load and full-load conditions.



Fig. 7. Magnetic flux lines and color map for a six-pole IM in no-load and full-load conditions.

1%. The growth is less pronounced for lower terminal voltages (i.e., weaker fluxes) because saturation effects in the rotor yoke are reduced.

In conclusion, the experimental tests confirm that, for a two-pole IM, a significant change may occur in the magnetizing current as a function of the slip due to the physical phenomenon quantitatively described in the previous subsection. A relatively traditional way to consider this fact in IM full-load power factor prediction employs FE time-harmonic simulations performed on the entire machine 2D model as discussed in the next Section.

*C. Machines With More Than Two Poles*

The phenomenon under study is specifically addressed for two-pole IMs in this paper. In fact, in machines having more than two poles, the main flux usually flows through the rotor from one pole to the next without crossing the solid-steel shaft, except in presence of significant saturation of the rotor yoke. Therefore, no remarkable rejection of flux lines from the shaft and no important increase in the yoke flux density when passing from no-load to on-load conditions are expected.

As an example, we can consider. Fig. 6 and Fig. 7, which compare the magnetic flux lines and the flux-density magnitude distributions in no-load and full-load conditions for the four-pole and six-pole IM's whose ratings and main data are provided in the Appendix A. It can be visually appreciated that the magnetic
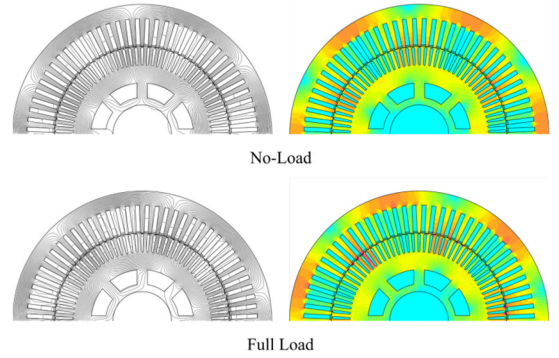


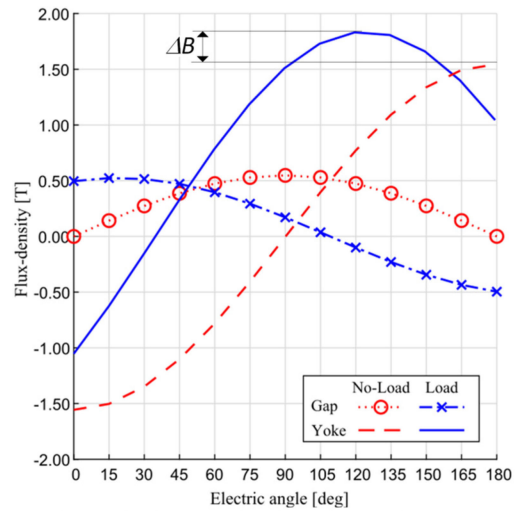Fig. 8. Flux-density fundamental distribution across the air-gap and rotor yoke midlines for a two-pole IM.

loading of the rotor yokes is practically not influenced by the slip, as there is no significant rejection of flux lines from the shaft into the rotor laminated core as a consequence of the rotor frequency change. Fig. 8, Fig. 9 and Fig. 10 show the flux-density fundamental distribution along the air-gap and rotor
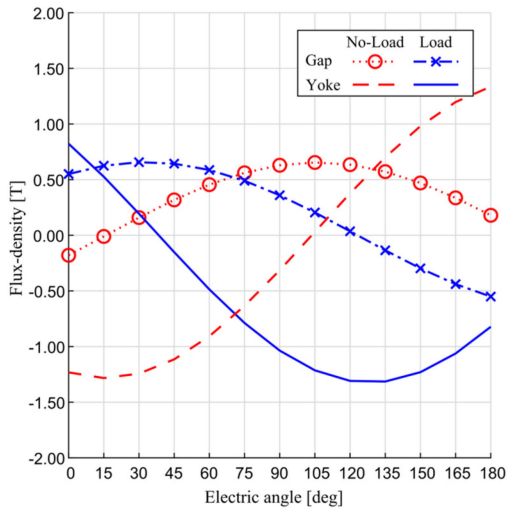
Fig. 9. Flux-density fundamental distribution across the air-gap and rotor yoke midlines for a four-pole IM.
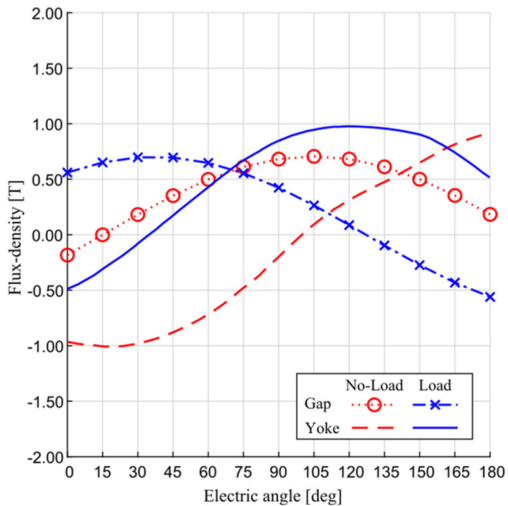


Fig. 10. Flux-density fundamental distribution across the air-gap and rotor yoke midlines for a six-pole IM.

yoke midlines in no-load and full-load conditions for the IMs in Fig. 2, Fig. 6 and Fig. 7, respectively. The air-gap plots consider the flux-density component normal to the midline, whereas the tangential component is taken along the yoke midline. It can be noticed that, for all the machines, the peak value of the air-gap flux-density is practically the same in both load and no-load conditions. Conversely, from Fig. 8 it is clear that the yoke flux-density increases (by a quantity indicated as $\Delta B$ in the figure) when the two-pole machine is loaded, whereas it remains the same in loaded and no-load conditions for the four-pole and the six-pole motors.

Incidentally, we can observe that in the case studies shown in Fig. 6 and Fig. 7, usual four-pole and six-pole designs with rotor axial cooling ducts are considered. However, simulations performed on the same machines in absence of cooling ducts and with similar saturation levels lead to the same behavior shown

in Fig. 6 and Fig. 7, i.e., to a negligible change in the rotor yoke flux density from no-load to on-load operation.

Instead, the phenomenon studied in the paper for two-pole IMs can actually occur also in IMs with a higher number of poles if the magnetic loading of the rotor is such that the rotor yoke is magnetically saturated or close to saturation [14]. Such a case is exemplified in Appendix B, where four- and six- pole IMs are considered with a rotor flux density above 1.3 T. The effect of shaft eddy currents at full load in medium-voltage IMs with more than two poles for different magnetic saturation levels will be studied in future works in more detail also based on experimental evidence.

## III. POWER FACTOR CALCULATION THROUGH STANDARD TIME-HARMONIC FE SIMULATION OF THE MACHINE 2D DETAILED MODEL

Time-stepping FE simulations are certainly a possible way to compute the full-load power factor of two-pole IMs with a solid-steel shaft [9]. However, they are known to be very time consuming. A faster but sufficiently accurate alternative, described in this Section, is an extension of the hybrid approach proposed in [13] such that analytical equivalent-circuit-based calculations are combined with 2D time-harmonic FE simulations performed on the detailed machine cross section at the slip frequency, taking shaft eddy-current effects into account. Actually, the complete model can be reduced exploiting the motor circumferential symmetry and limiting the analysis to one single pole; however, the full machine structure across a single pole needs to be modelled in detail, contrary to what is done with the new proposed approach described in Section IV.

### A. 2D Cross-Section Model Setting

Due to the 2D nature of the FE model, suitable provisions are needed to consider 3D effects that cannot be incorporated in it. In particular, the FE model axial length, according to [14], is set equal to $\hat{\ell}$ given by

$$\hat{\ell} = \ell + 2\delta - N_{\mathrm{cd}} \, w_{\mathrm{cd}} \, \frac{w_{\mathrm{cd}}}{5\delta + w_{\mathrm{cd}}} \qquad (1)$$

where $\ell$ is the total core length, $\delta$ is the air-gap width, $N_{\mathrm{cd}}$ is the number of stator cooling ducts and $w_{\mathrm{cd}}$ is their width. Equation (1) holds in the most usual case (for two-pole IMs) where cooling ducts are in the stator core only. If they are in the rotor too, then the meaning of symbols in (1) is defined according to [14].

As regards rotor bar conductivity, this is reduced with respect to its physical value to account for end rings. The equivalent conductivity $\hat{\gamma}_{\mathrm{rot}}$ assigned to the bars is determined so that the following equation holds:

$$\frac{1}{\hat{\gamma}_{\mathrm{rot}}} \frac{\hat{\ell}}{S_{\mathrm{bar}}} = \frac{1}{\gamma} \left[ \frac{\ell_{\mathrm{bar}}}{S_{\mathrm{bar}}} + \frac{\pi D_{\mathrm{ring}}}{2 Q_{\mathrm{r}} S_{\mathrm{ring}} \sin^2 \left( p \frac{\pi}{Q_{\mathrm{r}}} \right)} \right] \qquad (2)$$

where $\hat{\ell}$ is the FE model length defined by (1), $S_{\mathrm{bar}}$ is the bar cross section, $\gamma$ is the cage physical conductivity, $\ell_{\mathrm{bar}}$ is the bar length, $D_{\mathrm{ring}}$ is the ring average diameter, $Q_{\mathrm{r}}$ is the number of rotor bars, $S_{\mathrm{ring}}$ is the ring cross section and $p$ is the number
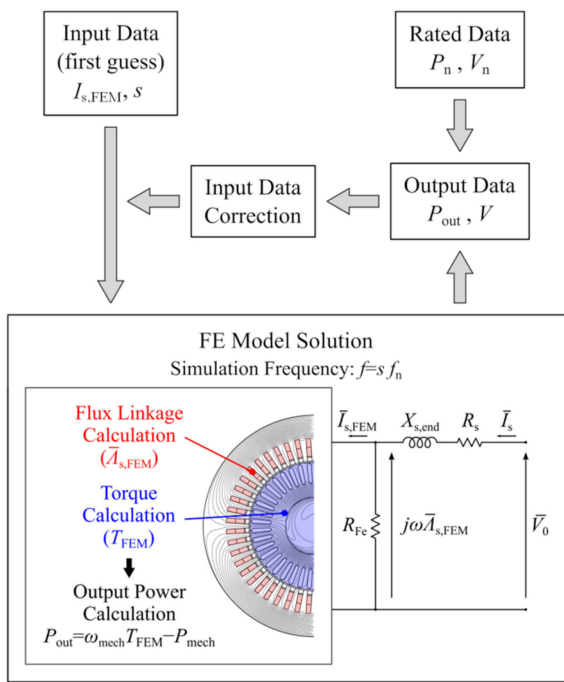
4

Fig. 11. Flowchart for full-load working point calculation based on time-harmonic FE analysis of the entire IM cross-section model.

of pole pairs ($p = 1$ for the purpose of this paper). The right-hand side of (2) is the total resistance of a squirrel cage portion including a single bar and the two ring elements connected to it as explained in [10].

As regards magnetic materials, both stator and rotor core laminations as well as the magnetic shaft need to be characterized by their B-H curves. The effect of laminations in stator and rotor cores is considered by properly adjusting their B-H curve through the stacking factor as suggested in [15]. Furthermore, the shaft region is assigned the electrical conductivity corresponding to the predicted working temperature.

### B. Solution Procedure

The computation procedure is represented by the flowchart in Fig. 11. It aims at determining the IM power factor during operation at rated voltage $V_\mathrm{n}$, rated power $P_\mathrm{n}$ and rated frequency $f_n$. For this purpose, an iterative process similar to that proposed in [16] is employed as described next.

The model is excited with a balanced three-phase current system of amplitude $I_\mathrm{s,FEM}$ and (slip) frequency $f = s f_\mathrm{n}$ being $s$ a first-guess rated slip. From the time-harmonic FE model solution the stator flux linkage complex phasor $\bar{\Lambda}_\mathrm{s,FEM}$ and the electromagnetic torque $T_\mathrm{FEM}$ are determined. The phase voltage phasor is then obtained as:

$$\bar{V}_0 = j2\pi f_\mathrm{n}\bar{\Lambda}_\mathrm{s,FEM} + (R_\mathrm{s} + jX_\mathrm{s,end})\,\bar{I}_\mathrm{s} \tag{3}$$

where $j$ is the imaginary unit, $R_\mathrm{s}$ the stator phase resistance, $X_\mathrm{s,end}$ the stator end-winding leakage reactance computed as

per [17] and $\bar{I}_\mathrm{s}$ the stator phase current phasor. The latter is:

$$\bar{I}_\mathrm{s} = I_\mathrm{s,FEM} + \frac{j2\pi f_\mathrm{n}\bar{\Lambda}_\mathrm{s,FEM}}{R_\mathrm{Fe}} \tag{4}$$

where $R_\mathrm{Fe}$ is the resistance usually included in the IM equivalent circuit to account for core losses [13]. The output power and line voltage are then obtained as:

$$P_\mathrm{out} = T_\mathrm{FEM}\omega_\mathrm{mech} - P_\mathrm{mech} = 2\pi f_\mathrm{n}\left(1 - s\right)T_\mathrm{FEM} - P_\mathrm{mech} \tag{5}$$

$$V = k\left|\bar{V}_0\right| \tag{6}$$

where $\omega_\mathrm{mech}$ is the rotor speed, $P_\mathrm{mech}$ represents mechanical (friction and windage) losses and coefficient $k$ is equal to either $\sqrt{3}$ or 1 depending on whether phases are star or delta connected, respectively.

The output data estimated from (5) and (6) are compared to the IM rated power $P_\mathrm{n}$ and voltage $V_\mathrm{n}$. If the difference is larger than a suitable tolerance, the phase excitation current $I_\mathrm{s,FEM}$ of the FE model and the slip $s$ are adjusted using a quasi-Newton algorithm [18] and the calculation procedure is repeated. More in detail the current and slip values to be used at the $(k + 1)$-th step of the algorithm ($I_{k+1}$, $s_{k+1}$) are deduced from the values at the $k$-th step as follows:

$$\begin{bmatrix} I_{k+1} \\ s_{k+1} \end{bmatrix} = \begin{bmatrix} I_k \\ s_k \end{bmatrix} + \mathbf{J}_k \begin{bmatrix} V_k - V_\mathrm{n} \\ P_k - P_\mathrm{n} \end{bmatrix}, \tag{7}$$

being $\mathbf{J}_k$ the inverse of the jacobian matrix of the model transfer function. At the beginning, this $2 \times 2$ matrix has to be evaluated numerically, calculating the voltage and power changes corresponding to small current and slip changes, respectively, while the remaining input is constant. From the second step on, [18] allows one to update the inverse jacobian matrix $\mathbf{J}_k$ at the $k$-th step using its value $\mathbf{J}_{k-1}$ at the previous step as follows:

$$\mathbf{J}_k = \mathbf{J}_{k-1} + \frac{\delta\mathbf{x}_k - \mathbf{J}_{k-1}\delta\mathbf{y}_k}{\delta\mathbf{x}_k^T\,\mathbf{J}_{k-1}\,\delta\mathbf{y}_k}\delta\mathbf{x}_k^T\,\mathbf{J}_{k-1} \tag{8}$$

where $T$ indicates transposed, $\delta\mathbf{x}_k = \begin{bmatrix} I_k - I_{k-1} & s_k - s_{k-1} \end{bmatrix}^T$ and $\delta\mathbf{y}_k = \begin{bmatrix} V_k - V_{k-1} & P_k - P_{k-1} \end{bmatrix}^T$. The iteration loop ends when the percent error between rated and estimated power and voltage values is below the chosen threshold.

The IM power factor at rated conditions is finally computed as the cosine of the angle between the phase voltage and current phasors given by (3) and (4).

## IV. NEW POWER FACTOR CALCULATION METHOD BASED ON A REDUCED FE MODEL

The computation procedure described in the previous Section, even faster than a time-stepping FE simulation, suffers from a relatively poor computational performance because it implies solving non-linear time-harmonic FE simulations of the entire IM, which are time-consuming. Instead, the new proposed approach to the problem, presented in this Section, employs a reduced IM 2D model, which will be shown to yield remarkable savings in terms of computation time without significant loss of accuracy.
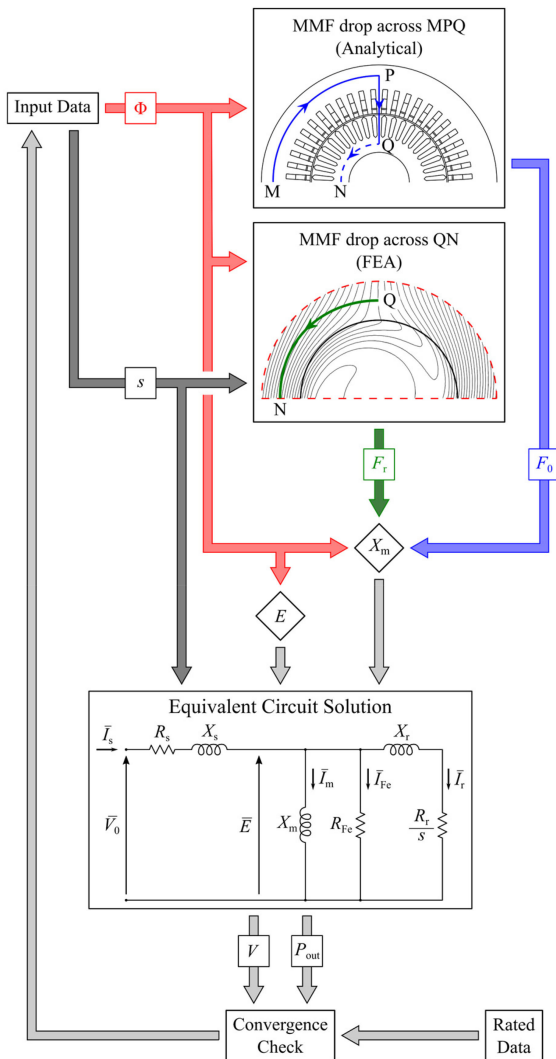
Fig. 12. Flowchart of the proposed procedure to determine the IM full-load operating point considering shaft eddy-current effects.



Fig. 13. (a) Complete IM model solved in no-load conditions; (b) reduced model solved at full-load slip frequency.

## A. Overall Procedure Description

The proposed procedure is illustrated in Fig. 12. As in the previous Section, the objective is to determine the IM working point (and, in particular, the power factor) in rated conditions (voltage $V_{\mathrm{n}}$, frequency $f_{\mathrm{n}}$ and output power $P_{\mathrm{n}}$) considering shaft eddy-current effects.

As a starting point, it is assumed that the IM operates with a first-guess flux per pole $\Phi$ and slip $s$. Then, the MMF drop $F_0$ across the contour $MPQ$ shown in Fig. 13-a (where the arc $MP$ develops along the stator yoke midline and $PQ$ crosses the stator and rotor teeth and the air gap) is analytically estimated. Such MMF drop is computed in no-load conditions for the assumed flux per pole $\Phi$ as:

$$F_0 = \int_{MPQ} \mathbf{H} \cdot \mathbf{d\ell}, \tag{9}$$

where $\mathbf{H}$ is the magnetic field vector and $\mathbf{d\ell}$ is the elementary vector representing an infinitesimal portion of the contour $MPQ$. The computation of (7) follows the analytical procedure
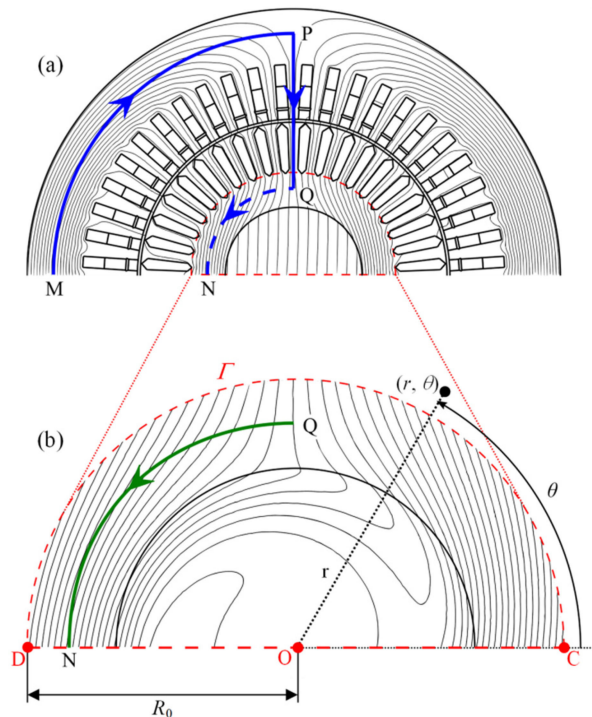
described in [11] to estimate the no-load magnetizing current for any given flux per pole. It will be assumed in the following that the MMF drop $F_0$ is the same in both no-load and full-load conditions. This is a reasonable hypothesis because the shaft eddy currents arising at full load produce a flux density increase in the rotor yoke (i.e., along the arc $QN$ in Fig. 13) but do not significantly alter the flux density (and hence the magnetic field $\mathbf{H}$) in the other IM cross-section regions.

What varies with rotor slip $s$ (hence from no-load to loaded conditions) is, instead, the MMF drop $F_{\mathrm{r}}$ across the arc $QN$ placed along the rotor yoke midline:

$$F_{\mathrm{r}} = \int_{QN} \mathbf{H} \cdot \mathbf{d\ell}. \tag{10}$$

For an accurate and sufficiently fast computation of $F_{\mathrm{r}}$, it is herein proposed to perform a time-harmonic FE simulation of the very simple semi-circular model shown in Fig. 13-b in order to reproduce the behavior of the rotor yoke and shaft in full load conditions (rated slip). The details on how such reduced model is built and solved will be separately provided in the next subSection (IV.B) for the sake of clarity.

After both $F_0$ and $F_{\mathrm{r}}$ are calculated, it is possible to estimate the IM full-load magnetizing current $I_{\mathrm{m}}$ and, from it, the full-load magnetizing reactance $X_{\mathrm{m}}$. In fact, the RMS value of the magnetizing current can be written as [14]:

$$I_{\mathrm{m}} = \frac{\pi}{3\sqrt{2}} \frac{p\left(F_0 + F_{\mathrm{r}}\right)}{k_{\mathrm{w}} N_{\mathrm{s}}} \tag{11}$$

where $k_{\mathrm{w}}$ is the stator winding factor and $N_{\mathrm{s}}$ is the number of series-connected turns per phase. Since the RMS value of motor

internal voltage $E$ across the magnetizing inductance (Fig. 12) is:

$$E = |\bar{E}| = \sqrt{2}\pi k_w N_s \Phi f_n, \tag{12}$$

the value of $X_m$ will be computed from (9) and (10) as:

$$X_m = \frac{E}{I_m} = 6k_w{}^2 N_s{}^2 \frac{\Phi f_n}{p(F_0 + F_r)} \tag{13}$$

At this point, the IM equivalent circuit shown in Fig. 12 can be solved to determine the line-to-line supply voltage $V$ and the output power $P_{out}$ as follows:

$$V = k|\bar{V}_0| = kE|1 + \bar{Z}_s/\bar{Z}| \tag{14}$$

$$P_{out} = \frac{3s(1-s)E^2 R_r}{R_r{}^2 + X_r{}^2 s^2} \tag{15}$$

where $k$ is equal to either $\sqrt{3}$ or 1 depending on the phase connection, $\bar{Z}_s$ is

$$\bar{Z}_s = R_s + jX_s \tag{16}$$

and $\bar{Z}$ is the total impedance across which the air-gap voltage $\bar{E}$ is applied in the single-phase equivalent circuit (Fig. 12):

$$\bar{Z} = \frac{-R_{Fe}X_m X_r s + jR_{Fe}R_r X_m}{R_{Fe}R_r - X_m X_r s + j(R_r X_m + R_{Fe}X_m s + R_{Fe}X_r s)} \tag{17}$$

In (13)–(15), the equivalent circuit parameters $R_s$ (stator resistance), $X_s$ (stator leakage reactance), $R_r$ (stator-referred rotor resistance), $X_r$ (stator-referred rotor leakage reactance) and $R_{Fe}$ (equivalent resistance accounting for core losses) are computed analytically with standard methods [10], [17].

The supply voltage and output power (12) and (13) are finally compared to the relevant rated values $V_n$ and $P_n$. If the relative error is below a fixed threshold the procedure is terminated, otherwise it is reiterated by adjusting the input values (slip $s$ and flux per pole $\Phi$) through a quasi-Newton algorithm [18].

When the iteration loop is terminated, the power factor is computed as the cosine of the argument of the complex impedance $\bar{Z} + \bar{Z}_s$ given by (14)-(15).

### B. Reduced IM Model for Time-Harmonic FE Analysis

This subsection describes the definition of the reduced model (Fig. 13-b) which needs to be solved by time-harmonic FEA at any iteration of the procedure described in IV.A.

For the sake of clarity let us define the polar coordinates $r$ and $\theta$ as shown in Fig. 13-b. The time-harmonic FE simulation, run at the rotor slip frequency $sf_n$, aims at determining a time-independent complex function $\bar{A}(r,\theta)$ such that the vector potential $A_z(r,\theta,t)$ at time $t$ and coordinates $r$ and $\theta$ in the model domain is given by [12]:

$$A_z(r,\theta,t) = \text{Re}\left\{\bar{A}(r,\theta)e^{j2\pi sf_n t}\right\} \tag{18}$$

Suitable boundary conditions in terms of $\bar{A}(r,\theta)$ need to be imposed on the model contour, which is composed of the arc $\Gamma$ and the two segments OD and OC. Regarding the segments OD and OC, they delimit one pole pitch and, therefore, anti-periodic

boundary conditions are applied to them [19], i.e.,:

$$\bar{A}(r,0) = -\bar{A}(r,\pi), \quad 0 \le r \le R_0, \tag{19}$$

being $R_0$ the radius of the arc $\Gamma$ which delimits the rotor yoke (Fig. 13-b).

Regarding $\Gamma$, the hypothesis is made that the flux density (and hence the vector potential) has a sinusoidal spatial distribution along it. The vector potential on $\Gamma$ will therefore take the form:

$$A_z(R_0,\theta,t) = A_0 \cos(\theta - 2\pi sf_n t). \tag{20}$$

The constant $A_0$ can be determined observing that the flux per pole $\Phi$ across the mean air-gap circumference is almost the same as the flux per pole entering the rotor yoke across $\Gamma$. The difference is due to the flux leakage through the rotor slots, which is usually neglected for the magnetizing current computation. Hence, we can write the flux crossing $\Gamma$ as:

$$\Phi \cos(2\pi sf_n t) \tag{21}$$

but also, using (18), as:

$$\hat{\ell}[A_z(R_0,0,t) - A_z(R_0,\pi,t)] = 2\hat{\ell}A_0 \cos(2\pi sf_n t). \tag{22}$$

being $\hat{\ell}$ the model axial length defined by (1). By equaling (19) and (20) we can determine $A_0$ as:

$$A_0 = \frac{\Phi}{2\hat{\ell}} \tag{23}$$

From (16), (18) and (21), the boundary condition on $\Gamma$ is therefore defined by assigning the complex vector potential values for $r = R_0$ as follows:

$$\bar{A}(R_0,\theta) = \frac{\Phi}{2\hat{\ell}}e^{-j\theta}, \quad 0 \le \theta \le \pi \tag{24}$$

Once boundary conditions are set based on the estimated value of the flux per pole $\Phi$, the model is solved through a time-harmonic FEA at the estimated slip frequency $sf_n$. From the solution, (8) is used to compute the estimated on-load MMF drop $F_r$ to be used in the following of the procedure (Fig. 13).

## V. EXPERIMENTAL VALIDATION

In order to assess the validity of the proposed calculation method a set of built and tested medium-voltage two-pole induction motors of different sizes is considered. Their ratings and some characteristic dimensions are given in Table II. Table III collects the equivalent circuit data for the six motors (identified as M1, M2, …, M6) listed in Table II; in this table the on-load magnetizing reactance, calculated as discussed in Section IV, is also shown.

All motors are for S1 service, have insulation class F and are equipped with solid a steel shaft. They have all undergone a full factory test according to [20]. Load tests have been conducted at rated load, and the power factor has been determined through a digital wattmeter from the measured voltage $V$, current $I$ and input electrical power $P_{in}$ as follows:

$$\cos\varphi = \frac{P_{in}}{\sqrt{3}\,V\,I} \tag{25}$$

TABLE II
SAMPLE MOTORS FOR EXPERIMENTAL VALIDATION

| Machine label | M1 | M2 | M3 | M4 | M5 | M6 |
|---|---|---|---|---|---|---|
| Shaft height [mm] | 315 | 355 | 400 | 450 | 500 | 630 |
| Rated power [MW] | 0.25 | 0.45 | 0.36 | 1.15 | 1.56 | 2.55 |
| Rated voltage [kV] | 4.0 | 4.0 | 6.6 | 4.0 | 4.0 | 11.0 |
| Rated current [A] | 42 | 75 | 37 | 187 | 257 | 154 |
| Rated frequency [Hz] | 60 | 60 | 50 | 60 | 60 | 50 |
| Rated power factor [ - ] | 0.88 | 0.89 | 0.88 | 0.90 | 0.90 | 0.89 |
| Total mass [t] | 1.7 | 2.4 | 3.5 | 5.0 | 6.9 | 12.5 |
| Core length [mm] | 420 | 420 | 420 | 600 | 600 | 950 |
| Outer stator diam. [mm] | 546 | 620 | 700 | 780 | 865 | 1080 |

TABLE III
EQUIVALENT CIRCUIT DATA

| Machine label | M1 | M2 | M3 | M4 | M5 | M6 |
|---|---|---|---|---|---|---|
| $R_s$ [$\Omega$] | 0.611 | 0.341 | 1.412 | 0.089 | 0.053 | 0.270 |
| $X_s$ [$\Omega$] | 10.965 | 4.930 | 19.537 | 2.015 | 1.873 | 7.526 |
| $R_r$ [$\Omega$] | 0.254 | 0.144 | 0.426 | 0.049 | 0.040 | 0.151 |
| $X_r$ [$\Omega$] | 4.012 | 2.920 | 6.458 | 1.423 | 0.790 | 4.822 |
| $R_{Fe}$ [$\Omega$] | 7592 | 5275 | 16957 | 2316 | 1766 | 7269 |
| $X_m$ – No load [$\Omega$] | 244.7 | 149.7 | 422.9 | 72.5 | 54.7 | 246.6 |
| $X_m$ – On load [$\Omega$] | 208.6 | 120.2 | 367.1 | 56.4 | 47.6 | 42.5 |
| Mech. losses [kW] | 5.53 | 12.25 | 8.44 | 28.33 | 42.47 | 88.39 |



Fig. 15. Stator line current from test and calculations.



Fig. 16. Slip from test and calculations.



Fig. 17. Magnetizing currents, obtained from no-load test (No-Load) and calculated from the I-ECM (On-Load), in per unit of the rated current.
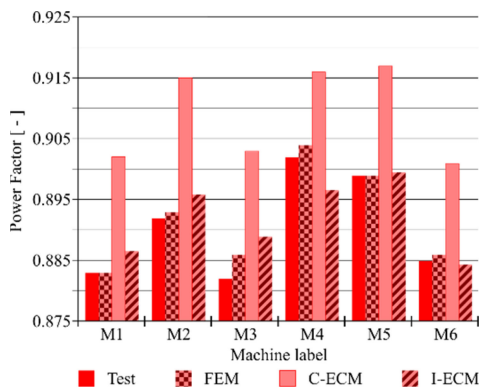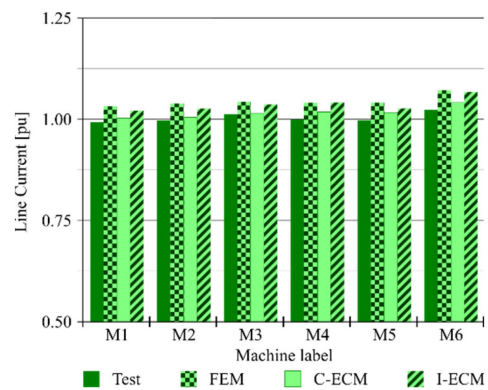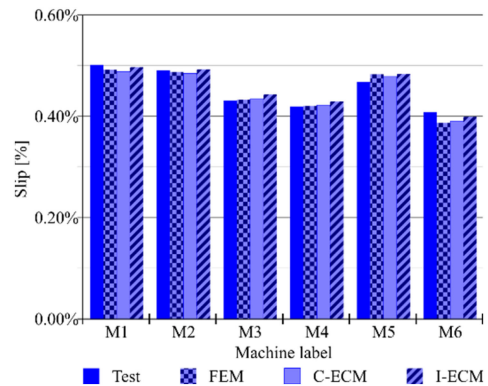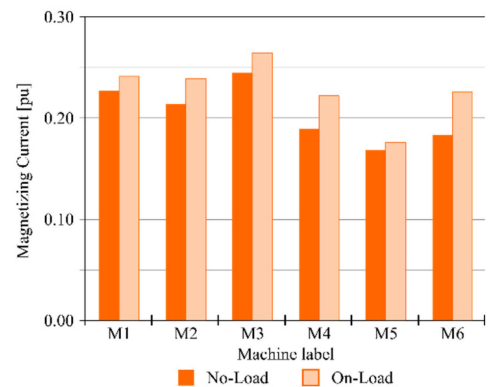


Fig. 14. Power factor from test and calculations.

For the purpose of validation and comparison, the full-load performance for all the IMs in Table II is computed with the following three independent methods: Finite-Element Method (FEM) based on the detailed machine 2D model, as described in Section III; Classic Equivalent Circuit Method (C-ECM) following the procedure described in [10], [11]; Improved Equivalent Circuit Method (I-ECM), employing a reduced machine 2D model, as described in Section IV. Power factor, line current and slip are predicted through the three methods.

Test and calculation results for the various quantities are shown in Fig. 14, Fig. 15 and Fig. 16. Fig. 17 shows the magnetizing current, as measured during the no-load test and predicted by calculation using the I-ECM.

It can be noticed how the three calculation methods being compared are generally equivalent and in good accordance with experimental data as far as the line current and slip prediction is concerned. Conversely, the power factor value obtained with the C-ECM appears much higher than that estimated using FEM and I-ECM. The results obtained with FEM and I-ECM are in good accordance between them and with measurements as far as the power factor prediction is concerned. It is therefore confirmed

TABLE IV
ERRORS IN POWER FACTOR EVALUATION

| Machine label | Tolerance | FEM | C-ECM | I-ECM |
|---|---|---|---|---|
| M1 | 1.95% | 0.00% | 2.15% | 0.41% |
| M2 | 1.80% | 0.11% | 2.58% | 0.44% |
| M3 | 1.97% | 0.45% | 2.38% | 0.79% |
| M4 | 1.63% | 0.22% | 1.55% | 0.60% |
| M5 | 1.68% | 0.00% | 2.00% | 0.06% |
| M6 | 1.83% | 0.11% | 1.80% | 0.07% |

TABLE V
CALCULATION STATISTICS

| Machine label | FEM | | I-ECM | |
|---|---|---|---|---|
| | Nodes | Iterations | Nodes | Iterations |
| M1 | 27134 | 3 | 4183 | 1 |
| M2 | 36634 | 4 | 4165 | 2 |
| M3 | 33668 | 4 | 4208 | 1 |
| M4 | 51483 | 5 | 4161 | 2 |
| M5 | 53352 | 3 | 4174 | 2 |
| M6 | 81729 | 4 | 4183 | 1 |
| AVERAGE | 47333 | 4 | 4179 | 2 |
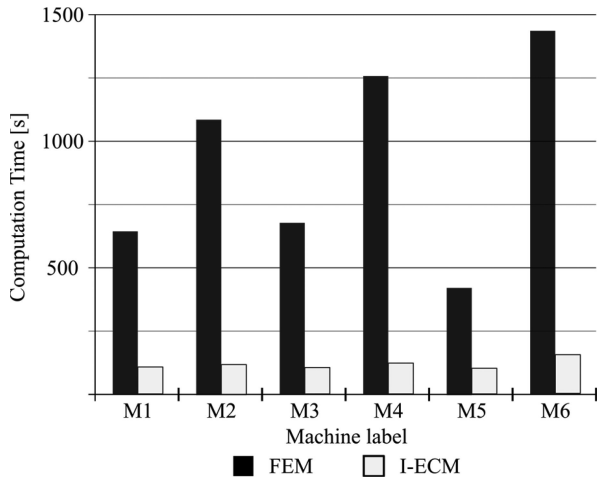


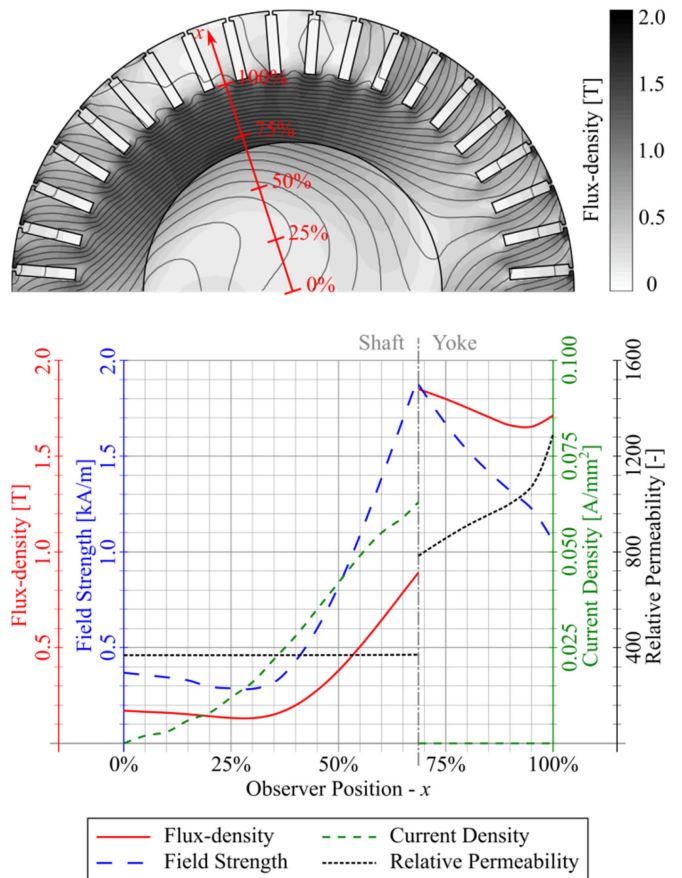Fig. 18. Computation time required to evaluate the correct on-load working point.



Fig. 19. Distribution of the flux density, magnetic field, magnetic permeability and eddy currents in the rotor of motor M3 (Table II) as obtained by FEA of the entire machine cross section.

that conventional analytical calculation techniques may lead to significant errors in the estimation of two-pole IMs equipped with solid-steel shaft.

In order to have a clearer assessment of the accuracy of the three compared methods, the percent errors in the prediction of the full-load power factor with respect to measurements are provided in Table IV. Table IV also shows the tolerance intended as the maximum error allowed in accordance to the IEC standard [6]. It can be noticed that, for most of the sample motors taken into account, the C-ECM overestimates the power factor with an error which exceeds the IEC tolerance. The errors for M4 and M6 are within the tolerance but, in any case, significantly larger than those affecting the other two computation methods.

Finally, Fig. 18 shows the total computation time for FEM and the I-ECM, in order to provide a quantitative assessment of the computational benefit resulting from the use of a reduced IM model (Section IV) instead of the complete one (Section III). All calculations are performed on the same workstation equipped with an Intel Core i5-3470@3.20 GHz processor (16 GB RAM), using a single-thread user-defined routine in Matlab. Table V reports other calculation statistics, i.e., the number of nodes of the 2D FE models (respectively complete and reduced) employed by the FEM and I-ECM for the various IMs, as well as the number of iterations required by the two methods to converge. In this regard, it is highlighted that, both for the FEM and the I-ECM, the iterative procedure starts with initial guess values (of the current, slip and flux per pole according to Fig. 12 and Fig. 13)

obtained analytically by solution of the conventional equivalent circuit.

It is clear from Fig. 18 and Table V that the I-ECM is much preferable to the FEM from a computational point of view, because it leads to a comparable level of accuracy with an average 10% demand in terms of computation time.

## VI. DISCUSSION

The time saving obtained with the proposed computation method (I-ECM) makes it more suitable than the FEM for being incorporated in genetic optimization programs for two-pole

IM design optimization [21], where hundreds or thousands of iterations may be requested to identify optimal design solutions.

With respect to purely analytical algorithms [8], [9], the method suffers from the drawback of requiring a time-harmonic 2D FEA, but this is applied to a very simple reduced motor model (Section IV-B) which can be built, solved and processed very quickly and in a fully-automated way. The convenience of solving such reduced FE model is explained by two main reasons. Firstly, it makes the procedure suitable for including the effect of axial cooling vents in the rotor core [7], [8], by simply adding them in the reduced FE model (Fig. 13-b). Secondly, it makes it possible to cope with the strongly non-uniform distribution of the magnetic-flux and eddy-current fields in the shaft and rotor yoke regions. An example in support to the latter point is shown in Fig. 19, which refers to the motor M3 in Table II. It is clear that the strongly non-uniform distribution of the magnetic field, flux density, magnetic permeability and eddy currents in the rotor core and solid-steel shaft is such that it would be extremely difficult to identify average or equivalent values for the mentioned quantities without a FEA (at least limited to the yoke and shaft domains as proposed in Section IV).

## VII. CONCLUSION

The computation of the full-load power factor for two-pole induction motors equipped with solid steel shaft is a critical task in the design of this kind of electrical machines. In fact, the eddy currents arising in the shaft in presence of a rotor slip tend to reject the main flux from the shaft region into the laminated rotor core, which therefore undergoes a stronger saturation than in no-load conditions. This causes the magnetizing current at full load to be larger than at no load, contrary to the common assumption made when predicting IM behavior with conventional equivalent-circuit-based analytical procedures. This paper has proposed a new computation approach which combines the equivalent circuit solution with the time-harmonic FEA of a very simple reduced 2D model of the IM, including only the rotor yoke and shaft region. The proposed approach has been validated by comparison against measurements on seven built and tested medium-voltage IMs of different sizes, showing that it can very accurately predict their full-load power factor. Compared to the FEA of the entire IM cross-sectional model, the method is proven to be much more computationally efficient while not causing any significant loss in the accuracy of results. On the other side, conventional analytical techniques based on equivalent circuit solutions without inclusion of shaft eddy-current effects are shown to result in a significant overestimation of the full-load power fact, with larger errors than allowed by some present international standards for IM testing.

Future work will be devoted to investigating eddy-current shaft effects on power factor estimation in medium-voltage IMs with more than two poles for different magnetic saturation levels of the rotor yoke. Computationally-efficient methods for IMs with higher number of poles will be then proposed and validated as an extension of the approach presented in this paper for the two-pole case.

TABLE VI
INDUCTION MOTOR DATA FOR COMPARISONS IN SECTION II-C

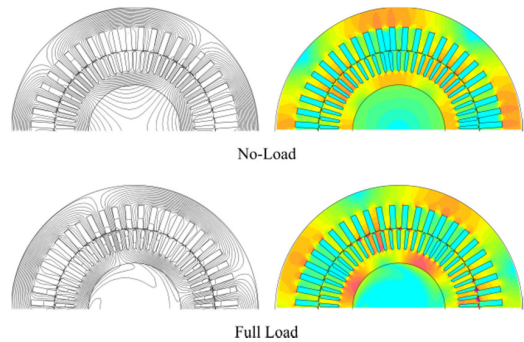| Number of poles | 2 | 4 | 6 |
|---|---|---|---|
| Rated power (kW) | 450 | 450 | 200 |
| Rated voltage (V) | 4000 | 4000 | 4000 |
| Rated current (A) | 78 | 73 | 34 |
| Rated frequency (Hz) | 60 | 60 | 60 |
| Rated power factor | 0.89 | 0.89 | 0.87 |
| Shaft height (mm) | 355 | 355 | 355 |
| Stator outer diameter (mm) | 620 | 620 | 620 |
| Stator core length (mm) | 380 | 460 | 340 |



Fig. 20. Magnetic flux lines and color map for a four-pole IM in no-load and full-load conditions with a no-load flux density in the yoke of 1.3 T.
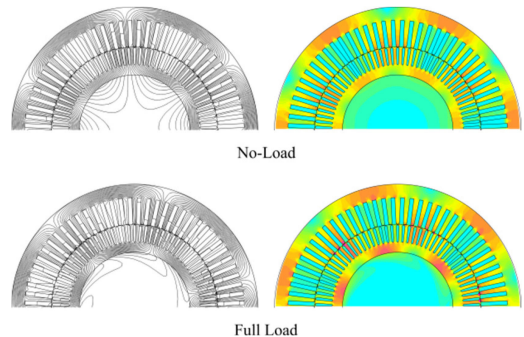


Fig. 21. Magnetic flux lines and color map for a six-pole IM in no-load and full-load conditions with a no-load flux density in the yoke of 1.3 T.

## APPENDIX A

In the following the main data for the three induction motors used for comparison in Section II-C are reported (Table VI).

## APPENDIX B

In this Appendix, FE simulations are used to investigate the behavior of four-pole and six-pole IMs (Fig. 20 and Fig. 21) designed with a no-load flux density in the rotor yoke of 1.3 T. In this case, the rotor yoke is moderately saturated even at no load and, as a consequence, a significant portion of the rotor flux is forced into the solid-steel shaft (Fig. 20 and Fig. 21).

When the machine is loaded and a slip frequency appears in the rotor, the eddy currents arising in the solid-steel shaft cause a rejection of the main flux lines causing the yokes to further saturate. This is confirmed by the plots in Fig. 22 and Fig. 23 which show how the flux density in the rotor yoke increases – exceeding 1.5 T – in loaded condition.
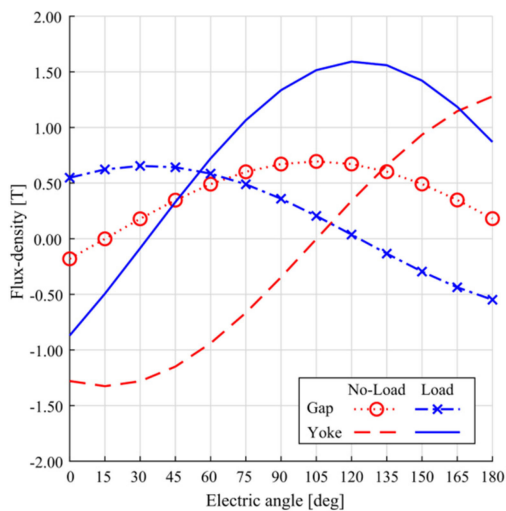
Fig. 22. Flux-density fundamental distribution across the air-gap and rotor yoke midlines for a four-pole IM with a no-load yoke flux density in the yoke of 1.3 T.
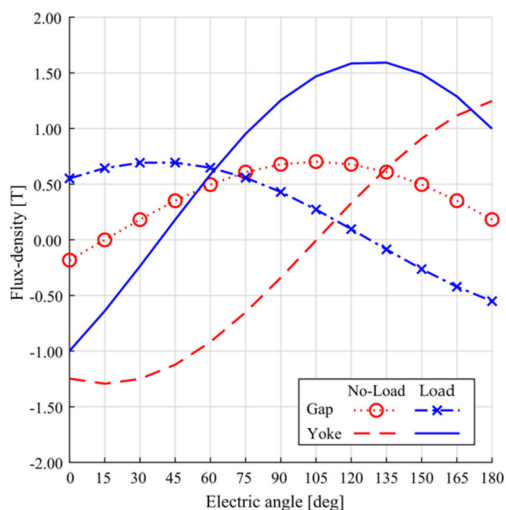


Fig. 23. Flux-density fundamental distribution across the air-gap and rotor yoke midlines for a six-pole IM with a no-load yoke flux density in the yoke of 1.3 T.

The presented simulations suggest that the phenomenon studied in this paper with regards to two pole-machines may actually occur also in IMs with a higher number of poles if they are designed with a relatively high value of no-load flux density in the rotor yoke.

The extension of the treatment and methodology proposed in this paper to IMs with more than two poles will be addressed and verified in future works providing adequate experimental validations.

## References

[1] D. F. Alexander, "Recent improvements in large induction motors," *J. A.I.E.E.*, vol. 46, no. 11, pp. 1167–1175, Nov. 1927.

[2] P. Zhang, Y. Du, T. G. Habetler, and B. Lu, "A survey of condition monitoring and protection methods for medium-voltage induction motors," *IEEE Trans. Ind. Appl.*, vol. 47, no. 1, pp. 34–46, Jan./Feb. 2011.

[3] A. T. de Almeida, F. J. T. E. Ferreira, and G. Baoming, "Beyond induction motors—Technology trends to move up efficiency," *IEEE Trans. Ind. Appl.*, vol. 50, no. 3, pp. 2103–2114, May/Jun. 2014.

[4] T. M. K. Yoon, C. S. Jeon, and S. K. Kauh, "Efficiency increase of an induction motor by improving cooling performance," *IEEE Trans. Energy Convers.*, vol. 17, no. 1, pp. 1–6, Mar. 2002.

[5] J. Parrish, S. Moll and R. C. Schaefer, "Synchronous versus induction motors: Plant efficiency benefits resulting from the use of synchronous motors," *IEEE Ind. Appl. Mag.*, vol. 12, no. 2, pp. 61–70, Mar./Apr. 2006.

[6] Rotating Electrical Machines–Part 1*: Ratings and Performance, IEC Standard 60034-1, 2017.

[7] R. D. Findlay, B. Szabados, S. H. Lie, S. J. Spencer, R. J. M. Belmans, and M. Poloujadoff, "Placement of vents to reduce shaft flux in two pole induction motors with a comment on heating effects," *IEEE Trans. Energy Convers.*, vol. 7, no. 3, pp. 483–490, Sep. 1992.

[8] M. Reinlein, T. Hubert, A. Kremser, and T. Bauer, "Magnetic flux distribution between rotor and shaft in two-pole induction machines with axial cooling vents," in *Proc. IEEE 5th Int. Conf. Power Eng., Energy Elect. Drives (POWERENG)*, Riga, 2015, pp. 485–490.

[9] M. Dems, K. Komeza, and J. Lecointe, "Influence of massive ferromagnetic shaft on the distribution of electromagnetic field and magnetising current for two- and four-pole induction motors at frequencies of 50 and 200 Hz," *IET Elect. Power Appl.*, vol. 12, no. 9, pp. 1407–1416, Nov. 2018.

[10] A. Boglietti, A. Cavagnino, and M. Lazzari, "Computational algorithms for induction-motor equivalent circuit parameter determination—Part I: Resistances and leakage reactances," *IEEE Trans. Ind. Electron.*, vol. 58, no. 9, pp. 3723–3733, Sep. 2011.

[11] A. Boglietti, A. Cavagnino, and M. Lazzari, "Computational algorithms for induction motor equivalent circuit parameter determination—Part II: Skin effect and magnetizing characteristics," *IEEE Trans. Ind. Electron.*, vol. 58, no. 9, pp. 3734–3740, Sep. 2011.

[12] N. Bianchi, *Electrical Machine Analysis Using Finite-Elements*. Boca Raton, FL, USA: CRC Press, 2005, p. 10, pp. 61–72.

[13] L. Alberti, N. Bianchi, and S. Bolognani, "A very rapid prediction of IM performance combining analytical and finite-element analysis," *IEEE Trans. Ind. Appl.*, vol. 44, no. 5, pp. 1505–1512, Sep./Oct. 2008.

[14] J. Pyrhönen, T. Jokinen, and V. Hrabovcová, *Design of Rotating Electrical Machines*, Chichester, UK: Wiley, 2008, pp. 153–224, p. 283.

[15] D. Meeker, Finite Element Method Magnetics User's Manual, version 4.2, Oct. 2015. [Online]. Available at: http://www.femm.info/wiki/Documentation/

[16] L. Alberti, N. Bianchi, and S. Bolognani, "Variable-speed induction machine performance computed using finite-element," *IEEE Trans. Ind. Appl.*, vol. 47, no. 2, pp. 789–797, Mar./Apr. 2011.

[17] A. Tessarolo and F. Luise, "An analytical-numeric method for stator end-coil leakage inductance computation in multi-phase electric machines," in *Proc. IEEE Ind. Appl. Soc. Annu. Meeting*, Edmonton, AB, 2008, pp. 1–8.

[18] C. Broyden, "A class of methods for solving nonlinear simultaneous equations," *Math. Comput.*, vol. 19, no. 92, pp. 577–593, Oct. 1965.

[19] S. J. Salon, *Finite Element Modeling of Electrical Machines*. Berlin, Germany: Springer Science, 1995.

[20] IEEE Standard Test Procedure for Polyphase Induction Motors and Generators, IEEE Standard 112, 2018.

[21] M. De Martin, F. Luise, S. Pieri, A. Tessarolo, and C. Poloni, "Numerical multi-objective optimization of a squirrel cage induction motor for industrial application," in *Proc. Intl Conf. Optim. Elect. Electron. Equip. (OPTIM) Intl Symp. Adv. Electromech. Motion Syst. (ELECTROMOTION)*, Side, Turkey, 2015, pp. 170–175.

**Matteo Olivo** received the Laurea degree from the University of Trieste, Trieste, Italy, in 2016 and the Ph.D. degree in electrical engineering from the University of Trieste, Italy, in 2019, where he is a Research Assistant. His research activity is focused on medium-voltage induction and synchronous machine design and analysis and is carried out in close cooperation with NIDEC Industrial Solutions, Monfalcone, Italy.

**Mauro Bortolozzi** received the Laurea and Ph.D. degrees in electrical engineering from the University of Trieste, Trieste, Italy, in 2012 and 2016, respectively. From 2016 to 2019, he was a Research Fellow with the University of Trieste, working in the field of electric machine design and optimization. Since 2019, he has been with Rete Ferroviaria Italiana, Trieste, where he deals with the design and management of the Italian railway electrical infrastructures. He is a Registered Professional Engineer in Italy and a member of the Italian Association of Electrical, Electronics, Automation, Information, and Communication Technology.

**Fabio Luise** received the Laurea and Ph.D. degrees in electrical engineering from the University of Padova, Padova, Italy, in 1999 and 2003, respectively. He joined NIDEC Industrial Solutions, Monfalcone, Italy, in 2004, as a permanent-magnet machine design Engineer. From 2008 to 2019, he led the motors and generators R&D team in the same company. Since 2019, he has been the Engineering Department Director for NIDEC Industrial Solutions. His research interests are in the field of conventional and innovative medium-voltage electric machinery.

**Alberto Tessarolo** received the Laurea and Ph.D. degrees in electrical Engineering from the University of Trieste, Trieste, Italy, in 2000 and 2011, respectively. Before joining the University, he worked in the design and development of large innovative motors, generators and drives. Since 2006, he has been with the Engineering and Architecture Department, University of Trieste, Italy, where he teaches the course of Electric Machine Design. He has authored more than 150 international papers in the area of electrical machines and drives. He has been an Associate Editor for the IEEE TRANSACTIONS ON ENERGY CONVERSION, IEEE TRANSACTIONS ON INDUSTRY APPLICATIONS and *IET Electric Power Applications*. He is an Editor-in-Chief of the IEEE TRANSACTIONS ON ENERGY CONVERSION.